Available online at www.sciencedirect.com
SCIENCE DIRECT®
Coordination Chemistry Reviews 245 (2003) 139–151
COORDINATION CHEMISTRY REVIEWS
www.elsevier.com/locate/ccr

Vectorial photoinduced electron-transfer in tailored redox-active proteins and supramolecular nanoparticle arrays

Itamar Willner*, Bilha Willner

Institute of Chemistry, The Farkas Center for Light-Induced Processes, The Hebrew University of Jerusalem, Givat Ram, Jerusalem 91904, Israel

Contents

Abstract

Vectorial electron transfer (ET) is a central feature of many biological transformations such as the photosynthetic apparatus or the biocatalytic oxygen assimilation. The present essay summarizes recent studies directed to the chemical modification of biomaterials to yield new photoactive materials that mimic natural photosynthesis to the extent that photoinduced directional ET leads to charge separation of the photogenerated redox products. Specifically, the reconstitution of proteins with photosensitizer–electron-acceptor units is addressed. One example involves the reconstitution of apo-myoglobin with a bis-bipyridinium Zn(II)-protoporphyrin dyad. Vectorial photoinduced ET initiated by the photoactive protein in the presence of the secondary electron acceptor $Ru(NH_3)_6^{3+}$ leads to substantial stabilization of the redox products. A second example includes the reconstitution of apo-β-hemoglobin with Co(II)-protoporphyrin IX as catalytic redox center and the chemical functionalization of the cysteine-93 residue with the eosin chromophore. The photogenerated redox species $Eo^{-\bullet}$–β-Hb–Co(I) are stabilized against back ET, $k_b = 370\ s^{-1}$. The modified protein acts as a photoenzyme for the photoinduced hydrogenation of acetylene to ethylene. A different approach to accomplish photoinduced vectorial ET involves the organization of layered Au-nanoparticle arrays crosslinked by the oligocationic bis-bipyridinium-Zn(II)-protoporphyrin IX (**1**), acting as a photosensitizer–electron-acceptor dyad. Photoinduced ET assembly leads to the transport of electrons through the conductive Au-nanoparticle array and to the generation of a photocurrent. A further approach to stimulate photoactivated vectorial ET involves the use of a photoisomerizable monolayer associated with an electrode as a command interface for the photochemical activation and deactivation of the electrical contact between cytochrome *c* (Cyt. *c*) and the electrode. A photoisomerizable monolayer consisting of pyridine and nitrospiropyran units is used to control the electrical contact between Cyt. *c* and the electrode. The electrically contacted Cyt. *c* activates the biocatalyzed reduction of O_2 by cytochrome oxidase (COx). The integrated system, consisting of the photoisomerizable monolayer-functionalized electrode and the Cyt. *c*/COx/O_2 components, provides a system for the amplified electrical transduction of photonic signals recorded by the monolayer interface. The system duplicates functions of the vision process.

Keywords: Photoinduced electron transfer; Artificial photosynthesis; Electron transfer in proteins; Au-nanoparticles; Photosensitizer–electron-acceptor dyad; Cytochrome *c*; Photoswitch; Photoactive monolayer; Functionalized electrode

* Corresponding author. Tel.: +972-2-658-5272; fax: +972-2-652-7715.
E-mail address: willnea@vms.huji.ac.il (I. Willner).

0010-8545/$ – see front matter © 2003 Elsevier B.V. All rights reserved.
doi:10.1016/S0010-8545(03)00068-7

1. Introduction

The photosynthetic apparatus is the most important biological process that converts light energy into chemical fuel products, Eq. (1).

$$nCO_2 + nH_2O \rightarrow (CH_2O)_n + nO_2 \quad (1)$$

The elucidation of the structural features of the photosynthetic reaction center, revealed the structure–function relationships and the mechanistic path leading to charge separation and light-to-electrical energy conversion [1,2], Fig. 1. The stepwise transfer of electrons from the primary photoexcited chromophore, bacteriochlorophyll, P_{LM}, to the series of electron acceptors, leads to spatial charge separation that retards the electron-hole recombination in the reaction center. The stabilization of the photogenerated redox species by means of the directional or vectorial electron transfer (ET) allows the secondary chemical utilization of the oxidized and reduced sites in thermodynamically 'uphill' fuel generating chemical transformations. Different chemical approaches were employed to mimic the primary charge separation events in the photosynthetic reaction center [3–5]. These include the synthesis of ingenious donor-photosensitizer–electron-acceptor triads or tetrads, where stepwise ET leads to spatial separation of the oxidized and reduced centers, and their stabilization against back ET [6]. A different approach to stabilize the ET photoproducts against back ET involves the organization of the chromophore and electron acceptor(s) components in microheterogeneous systems such as micelles [7], microemulsions [8], colloids [9] or zeolite systems [10]. Vectorial ET in these systems leads to the steric separation of the photogenerated redox products and their stabilization against back ET.

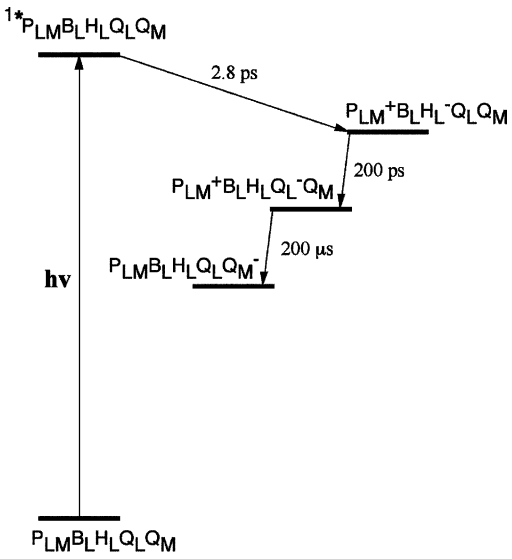

Fig. 1. Photoinduced vectorial ET and charge separation in the photosysnthetic reaction center. (P_{LM}—primary bacteriochlorophyll; B_L, B_M—secondary bacetriochlorophyll; H_L, H_M—bacteriopheophytin; Q_L, Q_M—quinone units).

2. Directional electron transfer in reconstituted proteins

Understanding ET in proteins has been a subject of extensive research efforts in the last 15 years. The functions of protein σ-bonds and intra-protein H-bonds in electron tunneling through the protein matrices, and the participation of amino acid residues as electron relay units for cooperative electron hopping and tunneling were discussed in detail [11–13]. We suggested the use of native proteins as predesigned structures for the assembly of semi-artificial photosynthetic reaction centers [14]. Several advantages may be identified by employing this approach: (i) Chromophores and catalytic sites may be introduced into selected positions of the protein by covalent attachment to appropriate amino acid residues (existing in the native protein or introduced by genetic engineering). Alternatively, cofactor units existing in the protein may be substituted by reconstitution processes. (ii) The protein provides a rigid matrix that could rigidify photosensitizer–electron relay units and thus facilitate charge separation. (iii) The introduction of catalytic sites into the protein may generate structurally-defined microenvironments that may lead to stereoselectivity and chiroselectivity in the respective chemical transformations. One method [15] to stimulate vectorial ET in protein assemblies is depicted in Fig. 2. The bis-bipyridinium-functionalized-Zn(II)-protoporphyrin IX (**1**), is a photosensitizer–electron-acceptor dyad. The flexibility of the molecular structure of (**1**) leads to efficient intramolecular quenching of the singlet excited state of the chromophore that eliminates the formation of the respective triplet-state of the Zn(II)-protoporphyrin IX. The generation of the photoactive photosensitizer–electron-acceptor protein assembly involves the elimination of the Fe(III)-protoporphyrin IX center from the native hemoprotein, myoglobin, to yield apo-myoglobin, apo-Mb. The reconstitution of apo-Mb with (**1**) yields the photoactive protein, where the rigidification of the photosensitizer–electron-acceptor in the protein leads to steric separation of the components that may facilitate charge separation. As the bipyridinium electron acceptor units generate a positively charged head group at the protein periphery, the coupling of the photosensitive protein to the secondary electron acceptor, $Ru(NH_3)_6^{3+}$ ($E^\circ = 0.083$ V vs. NHE), may lead to vectorial ET from the photogenerated primary bipyridinium radical cation ($E^\circ = -0.43$ V vs. NHE). The electrostatic repulsion of the reduced secondary relay unit, $Ru(NH_3)_6^{2+}$, from the protein surface may then enhance the stabilization of the redox products.

The lifetime of Zn(II)-protoporphyrin IX reconstituted into Mb is $\tau = 110$ s. From the shortening of the triplet lifetime in the ^{T}Zn(II)–V^{2+}–Mb as compared to the reference system Zn(II)–Mb, the intramolecular ET quenching rate constant, Eq. (2), is estimated to be $k_q = 1.55 \times 10^6$ s^{-1}. Fig. 3(A) curve (a) shows the transient corresponding to the recombination of the photogenerated products (followed at $\lambda = 670$ nm, corresponding to the absorbance of the oxidized species in the photogenerated products)

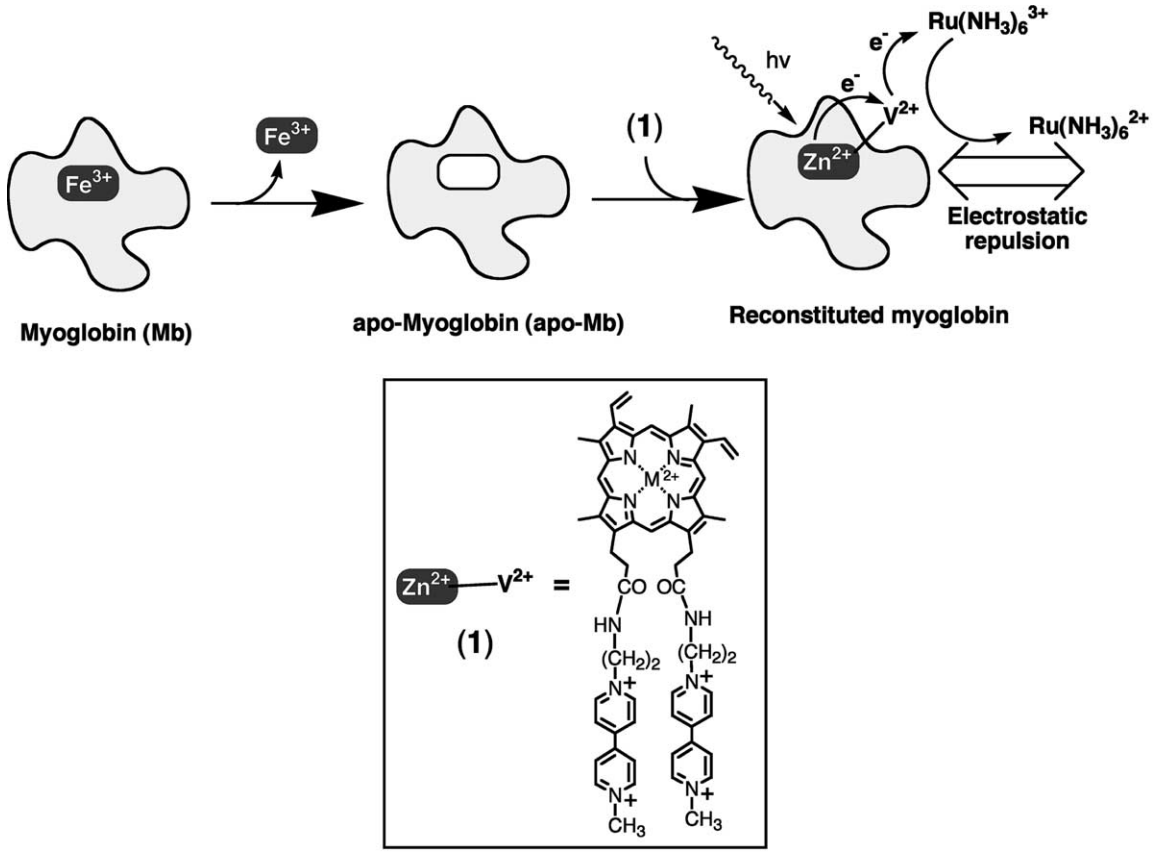

Fig. 2. Reconstitution of apo-Mb with the Zn(II)-protoporphyrin IX-bis-bipyridinium dyad (**1**).

Eq. (3). These experiments reveal that the reconstitution of the bis-bipyridinium-Zn(II)-protoporphyrin dyad into the apo-Mb retards the quenching process of the singlet state of the chromophore, probably by the rigidification of the dyad in the protein in an extended configuration that introduces a barrier for the intramolecular quenching. This feature of the photosensitive protein enables inter-system crossing to the triplet state and intramolecular ET, according to Eq. (2) and Eq. (3). Fig. 3(A), curves (b)–(d) shows the transients of the recombination process of the photogenerated dyad redox products (followed at $\lambda = 670$ nm corresponding to the absorbance of oxidized species in the photogenerated products) upon the addition of increasing amounts of the secondary electron acceptor, $Ru(NH_3)_6^{3+}$. An initial rapid decay of oxidized species Zn(II)–$P^{+\bullet}$ is observed, with a time constant characteristic to the recombination rate constant of Zn(II)–$P^{+\bullet}$–$V^{+\bullet}$–Mb in the absence of $Ru(NH_3)_6^{3+}$, Eq. (2). This fast transient is followed by the formation of a Zn(II)–$P^{+\bullet}$ species that essentially does not decay on the time-scale of decay of the photogenerated redox species in the dyad structure, but reveals a very slow decay process on a time-scale of seconds, Fig. 3(B). The concentration of the slow decaying component increases as the concentration of $Ru(NH_3)_6^{3+}$ is elevated. These results are rationalized in terms of a vectorial ET, where the photogenerated dyad reduces $Ru(NH_3)_6^{3+}$, Eq. (4). Electrostatic repulsion of the secondary reduced product from the protein periphery, and the shielding of the oxidized product by the protein, retards the recombination of the species, Eq. (5), and leads to the stability of the redox products.

$$^{*T}\text{Zn(II)–P–V}^{2+}\text{–Mb} \xrightarrow{k_q = 1.55\times10^6\ \text{s}^{-1}} \text{Zn(II)–P}^{+\bullet}\text{–V}^{+\bullet}\text{–Mb} \quad (2)$$

$$\text{Zn(II)–P}^{+\bullet}\text{–V}^{+\bullet}\text{–Mb} \xrightarrow{k_b = 1.3\times10^6\ \text{s}^{-1}} \text{Zn(II)–P–V}^{2+}\text{–Mb} \quad (3)$$

$$\text{Zn(II)–P}^{+\bullet}\text{–V}^{+\bullet}\text{–Mb} + \text{Ru}(\text{NH}_3)_6^{3+} \rightarrow \text{Zn(II)–P}^{+\bullet}\text{–V}^{2+}\text{–Mb} + \text{Ru}(\text{NH}_3)_6^{2+} \quad (4)$$

$$\text{Zn(II)–P}^{+\bullet}\text{–V}^{2+}\text{Mb} + \text{Ru}(\text{NH}_3)_6^{2+} \xrightarrow{k_b^1 = (6.5\pm0.5)\times10^7\ \text{M}^{-1}\,\text{s}^{-1}} \text{Zn(II)–P–V}^{2+}\text{Mb} + \text{Ru}(\text{NH}_3)_6^{3+} \quad (5)$$

The success in stabilizing photogenerated redox products against back ET by means of a protein matrix led us to an attempt to construct a semi-synthetic ‘photoenzyme’ [16]. The method to tailor the photoenzyme involves the modification of the protein by photosensitizer and electron-acceptor

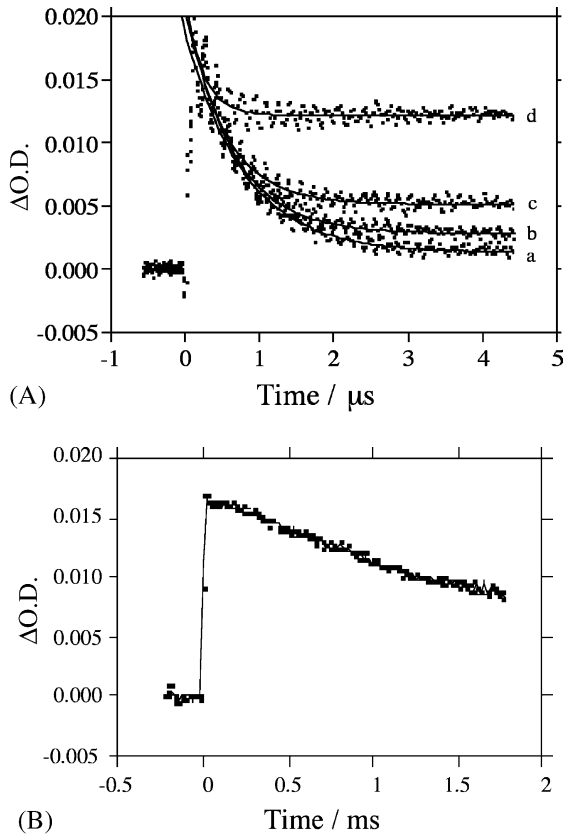

Fig. 3. (A) Transient corresponding to the recombination of the primary photoproducts Zn(II)–$P^{+\bullet}$–$V^{+\bullet}$–Mb in the absence of $Ru(NH_3)_6^{3+}$, curve (a), and in the presence of variable concentrations of $Ru(NH_3)_6^{3+}$-(b) 1×10^{-3} M; (c) 1×10^{-2} M; (d) 3×10^{-2} M. Recombination is followed at $\lambda=670$ nm (λ_{ex}=550 nm). (B) Transient decay of the long-lived photoproducts Zn(II)–$P^{+\bullet}$–V^{2+}–Mb and $Ru(NH_3)_6^{3+}$ generated by the vectorial ET.

units. By the application of an electron acceptor unit that exhibits catalytic properties upon the acceptance of an electron, photoinduced catalytic transformation may be driven. Proteins and specifically hemoproteins were reconstituted with synthetic photosensitizer and electron-acceptor units, and the photoinduced ET and charge separation in these systems was demonstrated [17]. Hemoglobin, Hb, is a tetrameric hemoprotein consisting of two α and two β subunits. In the present detailed example, the hemoglobin, Hb, composite tetramer was separated into its sub-components, and the heme site of the β-Hb-unit was substituted with Co(II)-protoporphyrin IX (**2**), according to Fig. 4(A). The single eosin maleimide chromophore, (**3**), was covalently linked to the cysteine-93 amino-acid residue, Fig. 4(A), to yield the photoactive photosensitizer-relay-functionalized protein. The photophysical characterization of the semisynthetic β-hemoglobin-derived protein reveals that upon photoexcitation of the eosin chromophore the excited triplet state transfers an electron to the Co(II)-protoporphyrin IX site, Eq. (6). By comparing the triplet lifetime of the eosin chromophore linked to β-apo-hemoglobin to the lifetime of the photosensitizer in the organized Eo^{2-}–β-Hb–Co(II) system, the intramolecular ET quenching rate-constant was estimated to be $k_q=1.8\times10^3\ s^{-1}$. Fig. 4(B) shows the transient corresponding to the back ET of the photogenerated redox species, Eq. (7), characterized by following the decay of the photogenerated Co(I) porphyrin at $\lambda=395$ nm. The recombination rate-constant corresponds to $k_b=370\ s^{-1}$. In the presence of the sacrificial electron donor, Na_2EDTA, the oxidized chromophore is reduced, Eq. (8), leading to the accumulation of the reduced Co(I) porphyrin.

$$^{T}Eo^{2-}\beta-Hb–Co(II) \xrightarrow{k_q=1.8\times10^3\ s^{-1}} Eo^{-\bullet}–\beta-Hb–Co(I)$$
$$\Delta G^\circ = -0.6\ eV \quad (6)$$

$$Eo^{-\bullet}–\beta-Hb–Co(I) \xrightarrow{k_b=370\ s^{-1}} Eo^{2-}–\beta-Co(II)$$
$$\Delta G^\circ = -1.7\ eV \quad (7)$$

$$Eo^{-\bullet}–\beta-Hb–Co(I) + Na_2EDTA \rightarrow Eo^{2-}–\beta-Hb–Co(I) + Na_2EDTA_{ox}$$
Decomposition products (8)

The distance between the eosin chromophore anchored to the cysteine residue in position 93 of β-Hb, and the reconstituted Co(II)-protoporphyrin IX is $d=12.87$ Å. The ET rate between a donor–acceptor pair is given by Marcus equation, Eq. (9), where d is the distance separating the donor–acceptor pair, d_o is the van der Waals distance between the reactants pair (ca. 3 Å), ΔG° and λ are the free energy change and the reorganization energy accompanying the ET process, respectively, $H_{AB}{}^\circ$ is the electronic coupling between the reactants, and β is the decay constant of the electronic coupling with distance. The redox potentials of the redox species participating in the ET in the photoenzyme Eo^{2-}–β-Hb–Co(II) are: $E^\circ(Co(II)/Co(I))=-0.61$ V; $E^\circ(Eo^{2-}/Eo^{-\bullet})=-0.90$ V and $E^\circ(Eo^{-\bullet}/Eo^{2-})=1.10$ V. These values translate to free energy changes accompanying the ET reactions summarized in Eqs. (6) and (7) of $\Delta G^\circ=-0.6$ and -1.7 eV, respectively. Assuming that the electronic coupling and its distance-dependent decay for the forward ET-quenching and recombination processes, Eqs. (6) and (7), are equal, the reorganization energy, λ, can be expressed in terms of Eq. (10), where $\Delta G_q{}^\circ$ and $\Delta G_b{}^\circ$ correspond to the free energy changes accompanying the ET transfer quenching, Eq. (6) and recombination, Eq. (7), respectively. Substitution of the respective values indicates that the reorganization energy associated with ET in the protein is $\lambda=1.1\pm0.1$ eV.

$$k_{ET} = \left(\frac{4\pi^3}{h^2\lambda k_B T}\right)^{1/2} \times H_{AB}^{\circ} \times \exp\{-\beta(d-d_o)\} \exp\left[\frac{\Delta G^o + \lambda)^2}{4\lambda k_B T}\right] \quad (9)$$

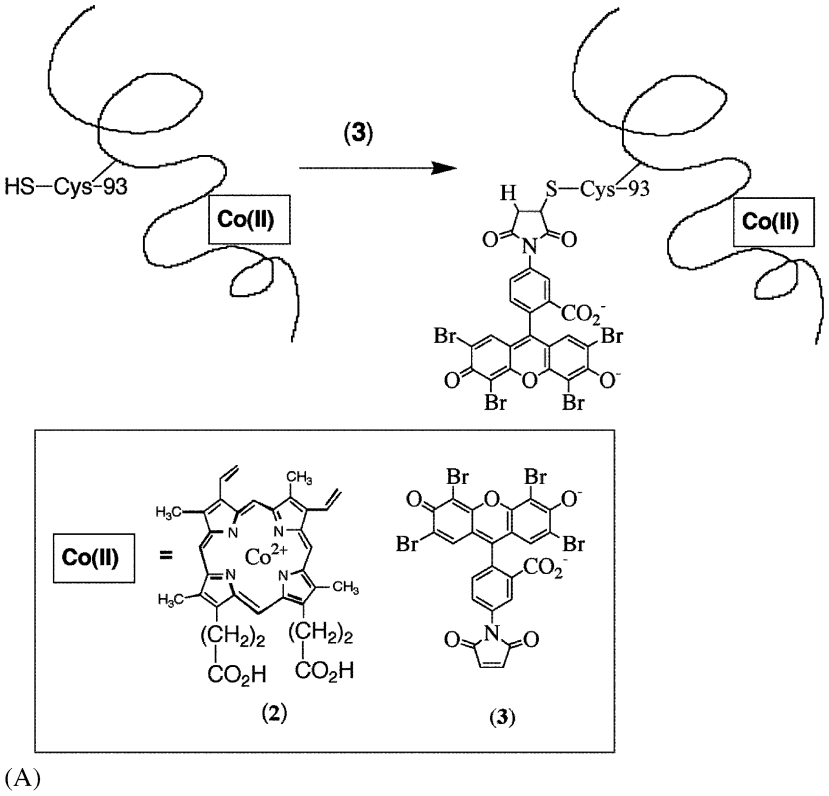

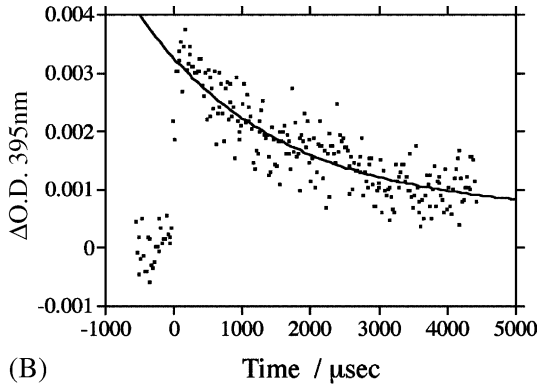

Fig. 4. (A) The reconstitution of apo-β-hemoglobin with Co(II)-protoporphyrin IX and its site-specific modification with the eosin photosensitizer. (B) Transient recombination of the photogenerated redox species $Eo^{-\bullet}$–β-Hb–Co(I) followed at $\lambda = 395$ nm ($\lambda_{ex} = 532$ nm).

$$\lambda = \frac{\Delta G_b^{\circ 2} - \Delta G_q^{\circ 2}}{4k_B T\left(\ln\frac{k_q}{k_b} - \frac{\Delta G_b^{\circ} - \Delta G_q^{\circ}}{2k_B T}\right)} \quad (10)$$

The reduction of the oxidized chromophore by the sacrificial electron donor, Na_2EDTA, Eq. (8), accumulates the reduced Co(I)-protoporphyrin center. The reduced species is depleted with time with the transformation of the metalloporphrin state to Co(III)-protoporphyrin IX. Furthermore, continuous irradiation of the Eo^{2-}–β-Hb–Co(II) photoenzyme reveals that hydrogen (H_2) is generated in the system. Accordingly, the formation of hydrogen and the depletion of the reduced Co(I)-protoporphyrin species are attributed to the transformation of the photogenerated Co(I) product to a Co(III)-hydride species that undergoes protonation to form H_2, Eq. (11).

$$Eo^{2-}\text{–}\beta - Hb\text{–}Co(I) \xrightarrow{H^+} Eo^{2-}\text{–}\beta - Hb\text{–}Co(III)\text{–}H \xrightarrow{H^+} Eo^{2-}\text{–}\beta - Hb\text{–}Co(III) + H_2 \quad (11)$$

Photogeneration of H_2 in the system proceeds, however, at a very low quantum yield, ca. 2×10^{-4}, although the reduced species in the system, Co(I)-protoporphyrin IX is formed at a substantially higher quantum yield that corresponds to $\phi = 1.4 \times 10^{-2}$. As the formation of the hydride is known to proceed efficiently, k ca. 10^9 M^{-1} s^{-1}, the experimental observation suggests that the protonation of the Co(III)-hydride is slow. Thus, the utilization of the hydride

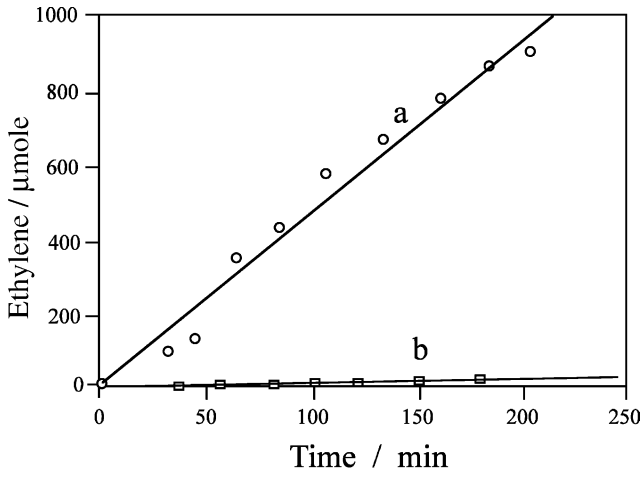

Fig. 5. Rate of light-induced hydrogenation of acetylene to ethylene by: (a) The Eo^{2-}–β-Hb–Co(II). (b) By diffusional eosin, Eo^{2-}, and β-Hb–Co(II). All experiments were performed in phosphate buffer, 0.1 M, pH 7.5, in the presence of Na_2EDTA, 1×10^{-2} M under acetylene.

in another chemical path (e.g. insertion of a substrate into the metal-hydride species), could lead to new photochemically driven chemical transformations. Indeed, irradiation of the Eo^{2-}–β-Hb–Co(II) and Na_2EDTA in the presence of acetylene results in the formation of ethylene, and the H_2 evolution process is fully blocked. Fig. 5, curve (a), shows the yield of the ethylene at time intervals of illumination. The quantum yield for ethylene formation is $\phi = 1 \times 10^{-2}$ ca. 50-fold higher than the yield of H_2 evolution in the absence of acetylene. Control experiments revealed that no ethylene is generated in the system in the dark or upon irradiation in the absence of Na_2EDTA. These control experiments imply that ethylene is generated by a light-induced process, and that the steady-state formation of the Co(I) (or Co(III)–H) product is essential. Accordingly, the production of ethylene is attributed to the insertion of acetylene into the Co(III)-hydride species, followed by the protonation of the alkenyl complex to ethylene, Eq. (12).

$$Eo^{2-}\text{–}\beta - \text{Hb–Co(III)–H} + C_2H_2 \rightarrow Eo^{2-}\text{–}\beta - \text{Hb–Co(III)–(CH=CH}_2) \xrightarrow{H^+} Eo^{2-}\text{–}\beta - \text{Hb–Co(III)} + CH_2{=}CH_2 \quad (12)$$

Fig. 5 curve (b), shows the rate of ethylene formation upon the irradiation of a reference system consisting of the eosin chromophore, Eo^{2-}, and Co(II)-protoporphyrin IX in the absence of the protein matrix. Only a trace amount of ethylene is formed. Time-resolved laser flash photolysis experiments reveal that no separated photoproducts are detected, indicating that the photoproducts $Eo^{-\bullet}$ and Co(I)-protoporphyrin IX species recombine on a sub-nanosecond time-scale. The rapid recombination of the diffusional species prevents the secondary chemical transformation, e.g. hydrogenation of acetylene. Thus, the assembly of the photosensitizer–Co(II)-protoporphyrin functional units yields an organized assembly where effective charge separation is accomplished. The catalytic function of the reduced species enabled us to tailor a 'photoenzyme' that drives the light-induced hydrogenation of acetylene.

3. Metal nanoparticle arrays crosslinked with transition metal complexes

3.1. Au-nanoparticle arrays crosslinked with a Pd(II)-square complex for sensor applications

Transition metal complexes might act as useful building blocks for the construction of functional nanostructures. Recent research efforts are directed to the 'bottom-up' organization of nanoparticle arrays on surfaces, aimed to generate nanoarchitectures of unique electronic, sensoric, optical and photoelectrochemical properties [18,19]. We applied oligocationic transition metal complexes as functional units for tailoring of layered arrays of citrate-capped Au-nanoparticles (diameter 12±1 nm) [20]. The Pd(II)-square complex $[(en)Pd(4,4'\text{-bipy})]_4(NO_3)_8$ (**4**), was applied to construct the layered Au-nanoparticle array, Fig. 6. A primary citrate-capped Au-nanoparticle layer was assembled on a positively-charged propylammonium siloxane film associated with transparent ITO glass surfaces. The resulting nanoparticle layer associated with the surface was then interacted with the oligocationic Pd(II)-square complex, (**4**), to yield the electrostatically linked metal complex on the nanoparticles. The interface was further reacted with the negatively-charged Au-particles to generate a second nanoparticle layer crosslinked to the first Au-nanoparticle layer by the Pd(II)-complex. Thus, by a stepwise deposition process a controlled number of Au-nanoparticle layers can be deposited on the surface. Fig. 7(A) shows the cyclic voltammograms of the Au-nanoparticles upon the build-up of the array. The cyclic voltammograms correspond to the reduction of the surface oxide layer associated with the particles and the back oxidation of the surface ions. It is evident that the amperometric responses of the Au-nanoparticle array increases as the number of Au-particle layers is elevated. Knowing the diameter of the nanoparticles (12±1 nm), and assuming that the voltammetric wave corresponds to the oxidation of all surface Au(I)-ions (and only the surface ions!), the surface coverage of the Au-nanoparticles correspond to 0.2×10^{11} particles cm^{-2} per layer. The fact that the voltammetric response of the layered array increases almost linearly with the number of layers implies that the array exhibits three-dimensional conductivity. It should be noted that the (**4**)-crosslinked array should not be considered as an ordered nanoparticle array but as an aggregated three-dimensional structure, where each layer is almost saturated with the Au-nanoparticles. Fig. 7(B) shows the absorbance spectra of the array upon the build-up of the nanoparticle array. We observe an increase in the plasmon absorbance at $\lambda = 518$ nm upon increasing the number of Au-nanoparticle layers.

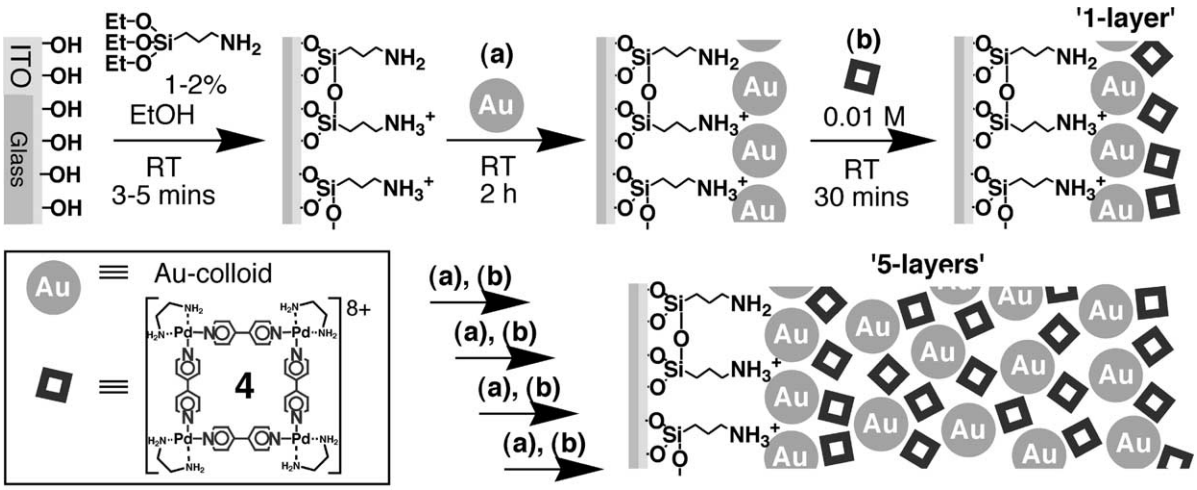

Fig. 6. The stepwise assembly of a layered Au-nanoparticle array using the Pd(II)-square complex (**4**) as crosslinker.

We also observe that upon increasing the number of Au-nanoparticle layers a new absorbance-band at $\lambda = 650$ nm is detected, and its intensity is enhanced as the number of layers is elevated. This absorbance band is attributed to an interparticle plasmon exciton coupling that is facilitated upon the aggregation of the nanoparticles. Thus, the optical properties of the nanoparticle array may be tuned by the number of Au-nanoparticle layers. While a low number of layers exhibit a red color, the surface turns blue when 6–8 layers of the nanoparticles are immobilized on the surface. The three-dimensional conductivity of the Pd(II)-square-crosslinked Au-nanoparticle array enables the electrochemical sensing of a redox-active substrate that is encapsulated in the transition metal complex unit. We find that *p*-hydroquinone binds to the Pd(II)-square complex, whereas *o*-hydroquinone lacks affinity for the crosslinking metal complex. This allowed the selective electrochemical sensing of *p*-hydroquinone in the concentration range that corresponds to 2×10^{-7} to 1.2×10^{-6} M. The selective binding of *p*-hydroquinone as compared to *o*-hydroquinone is explained by the accommodation of *p*-hydroquinone in a diagonal configuration in the Pd(II)-square, a binding motif that is not accessible to *o*-hydroquinone.

3.2. Au-nanoparticle arrays crosslinked with photosensitizer–electron-acceptor units for photoelectrochemical applications

The assembly of nanoparticles, especially semiconductor nanoparticles, attracts substantial research efforts directed to the preparation of photoelectrochemical functional systems [21]. The possibility of generating molecular crosslinked nanoparticle arrays was utilized to assemble nanoparticle arrays exhibiting photoelectrochemical functionalities [22]. The photoactive photosensitizer–electron-acceptor bis-bipyridinium-Zn(II)-protoporphyrin IX (**1**), was used as a polycationic crosslinking unit of Au-nanoparticle layers, Fig. 8. The base Au-nanoparticle layer, associated with a propylammonium siloxane film linked to an ITO electrode was reacted with (**1**) and then interacted with the Au-nanoparticles. Using a layer-by-layer deposition process a controlled number of Au-nanoparticle layers crosslinked by (**1**) is generated on the transparent ITO conductive glass support [21]. Fig. 9(A) shows the absorbance spectra of the (**1**)-crosslinked Au-nanoparticle array. The plasmon absorbance of the Au-nanoparticles, $\lambda = 518$ nm, increases in its intensity upon the build-up of the layers. The new

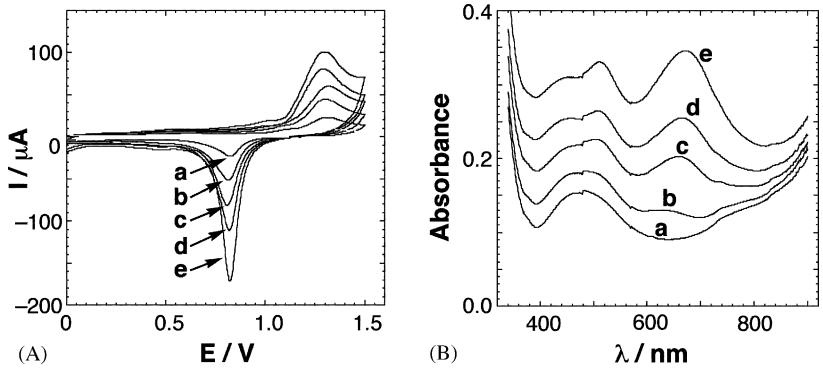

Fig. 7. (A) Cyclic voltammograms corresponding to the layered (**4**)-crosslinked Au-nanoparticle array upon the build-up of 1–5 Au-nanoparticle layers (curves (a)–(e)). Data recorded in 1.0 M H_2SO_4, scan rate 50 mV s^{-1}. (B) Absorbance spectra of the layered (**4**)-crosslinked Au-nanoparticle assembly consisting of 1–5 Au-nanoparticle layers (curves (a)–(e), respectively).

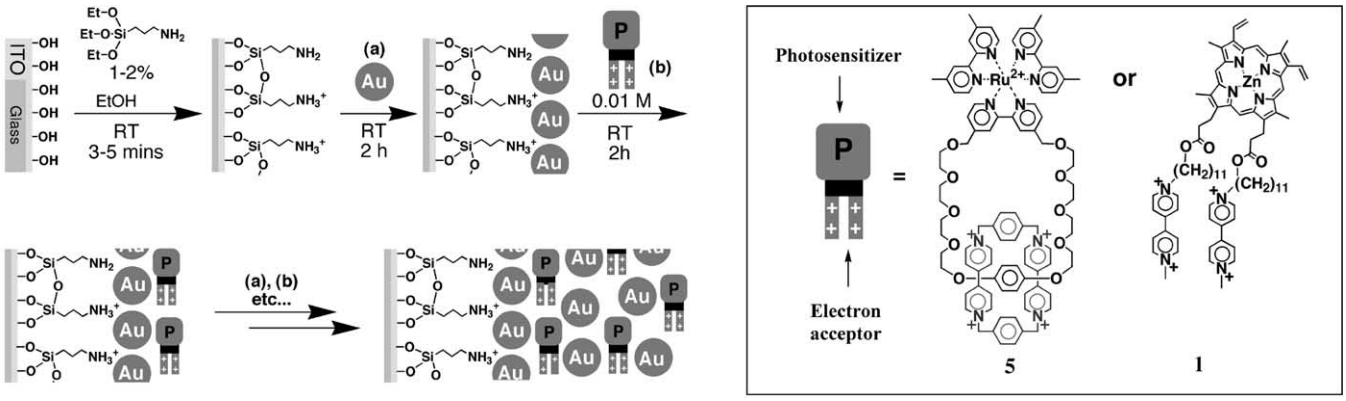

Fig. 8. The assembly of a layered Au-nanoparticle array crosslinked by the bis-bipyridinium-Zn(II)-protoporphyrin IX (**1**) or the catenated bis-bipyridinium cyclophane Ru(II)–tris-bipyridine (**5**) acting as photosensitizer–electron-acceptor dyads.

absorbance band at $\lambda = 650$ nm is intensified as the number of aggregated Au-nanoparticle layers is elevated. This band is attributed to the coupled interparticle plasmon excitation, a process that is facilitated as the aggregation of the particles is enhanced. Fig. 9(B) depicts the cyclic voltammograms of the bipyridinium sites of the crosslinking units upon the build-up of the Au-nanoparticle layers. The voltammetric response of the bipyridinium components increases almost linearly as the number of Au-nanoparticle layers is elevated. This implies that the Au-nanoparticle array exhibits three-dimensional conductivity, and that all molecular crosslinking units of (**1**) reveal electrical communication with the bulk ITO electrode through the Au-nanoparticles. Coulometric assay of the reduction (or oxidation) wave of the bipyridinium units indicates a surface coverage of (**1**) per layer that corresponds to 2×10^{11} mole cm^{-2}. Fig. 9(C) shows the cyclic voltammograms of the Au-nanoparticles upon the assembly of the (**1**)-crosslinked layers. By the coulometric assay of the oxidation wave of the surface-confined Au(I) ions, and knowing the size of the Au-nanoparticles, we estimate the surface coverage of the Au-particles to be 0.5×10^{11} particles cm^{-2} per layer. That is, ca. 250 units of the crosslinker (**1**) are associated with each particle in the crosslinked layered array. The electrostatic bridging of the particles by the many molecular crosslinking units leads to the high stability of the layered arrays. The layered Au-nanoparticle structures can be removed from the ITO plates only by physical scratching.

The photosensitizer–electron-acceptor-crosslinked Au-nanoparticle array exhibits photoelectrochemical activity. Fig. 10(A) shows the photocurrent action spectra of one- and four-layer (**1**)-crosslinked arrays of Au-nanoparticles resulting from the irradiation of the functionalized electrode in the presence of Na_2EDTA as sacrificial electron donor. The photocurrent spectrum follows the absorbance features of the Zn(II)-protoporphyrin IX chromophore, implying that the photocurrent originates from the photoexcitation of the Zn(II)-porphyrin chromophore. Fig. 10(B) shows the light-switchable photocurrents originating from the irradiation of (**1**)-crosslinked Au-nanoparticle arrays consisting of 4 layers. The photocurrent increases, albeit non-linearly, with the number of crosslinked Au-nanoparticle layers in the arrays. The photocurrent in the system is controlled by the potential applied on the electrode. At $E = -0.55$ V vs. SCE a sharp decrease in the photocurrent is observed, and at more negative potentials the photocurrent is fully depleted. That is, a sharp decrease in the photocurrent is observed

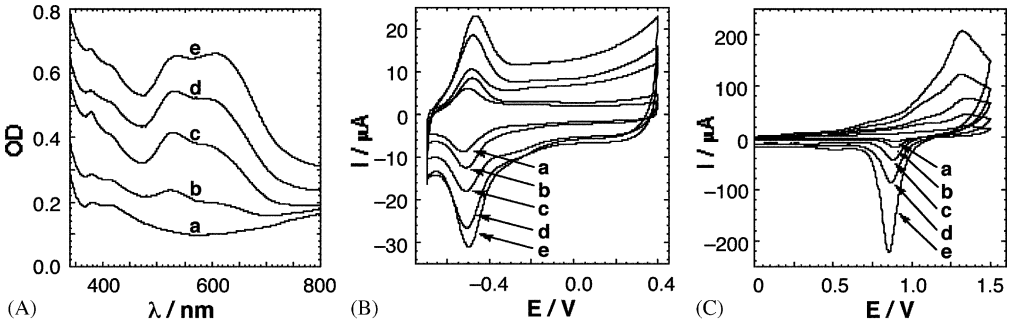

Fig. 9. (A) Absorbance spectra corresponding to the layered (**1**)-crosslinked Au-nanoparticle array, (a)–(e), 1–5 Au-nanoparticle layers. (B) Cyclic voltammograms corresponding to the bipyridinium units of the dyad (**1**) upon the build-up of 1–5 Au-nanoparticle layers (curves (a)–(e), respectively). Voltammograms were recorded under argon in 0.1 M phosphate buffer solution, pH 7.2, scan-rate 100 mV s^{-1}.(C) Cyclic voltammograms corresponding to the Au-nanoparticles in the layered (**1**)-crosslinked Au-nanoparticle assembly. Voltammograms (a)–(e) correspond to 1–5 Au-nanoparticle layers. Data were recorded in 1.0 M H_2SO_4, scan-rate 50 mV s^{-1}.

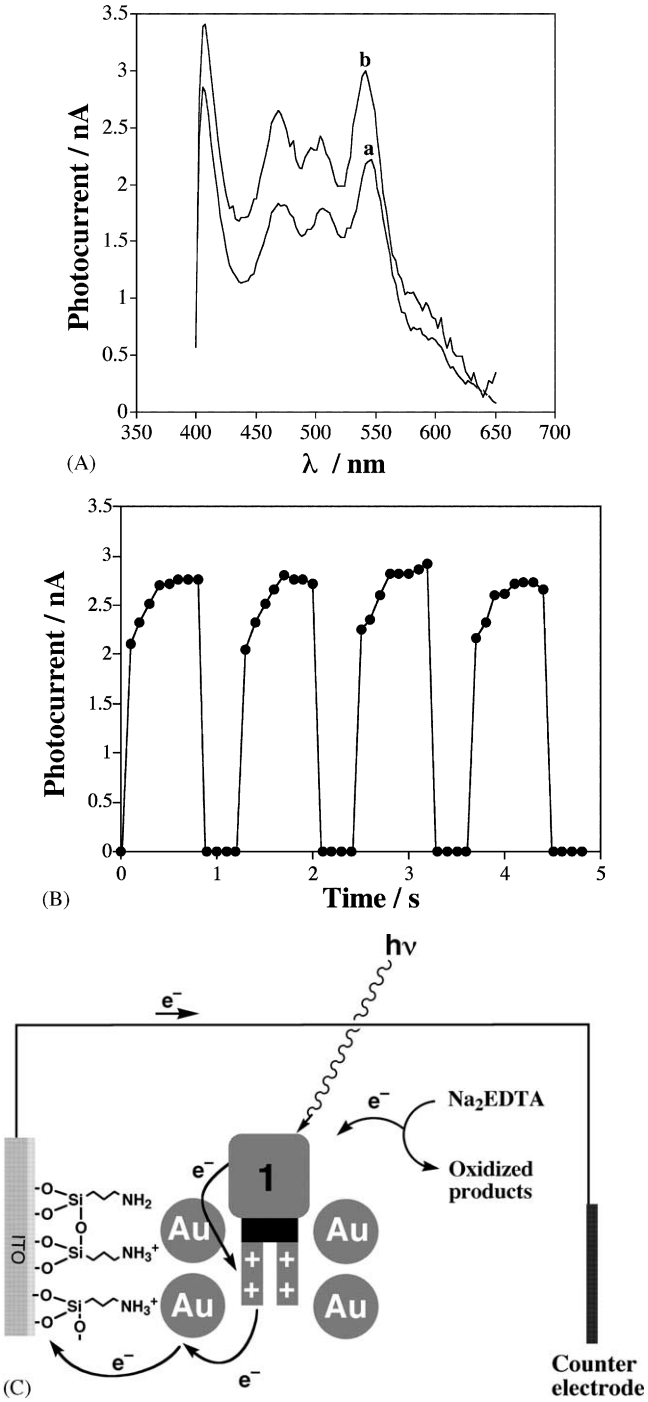

Fig. 10. (A) Photocurrent action spectra of (**1**)-crosslinked Au-nanoparticle structures associated with an ITO electrodes and consisting of: (a) One layer of Au-nanoparticles with electrostatically adsorbed (**1**). (b) A four-layer (**1**)-crosslinked Au-nanoparticle array. (B) Light-induced 'ON' and 'OFF' photocurrents of a four layer (**1**)-crosslinked Au-nanoparticle assembly associated with an ITO electrode. (Irradiation at $\lambda = 544$ nm). (C) Schematic photoinduced ET mechanism in the layered (**1**)-crosslinked Au-nanoparticle array leading to the generation of the photocurrent.

at the redox-potential characteristic to the bipyridinium units that crosslink the Au-nanoparticle array. This enables us to formulate the mechanism for the formation of the current in the system. Photoexcitation of the Zn(II) porphyrin IX

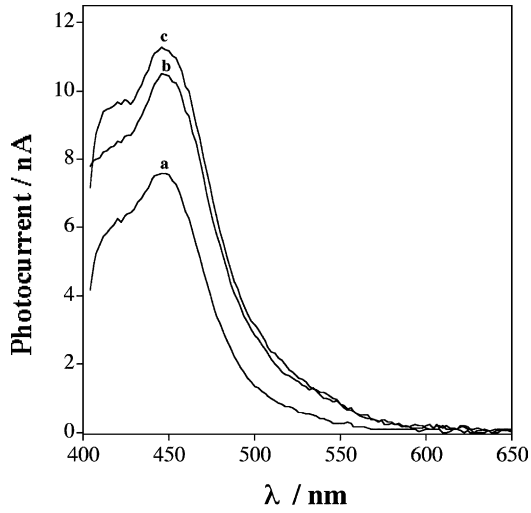

Fig. 11. Photocurrent action spectra generated by the layered (**5**)-crosslinked Au-nanoparticle array consisting of: (a) one, (b) three and (c) four nanoparticle layers.

chromophore results in the intramolecular ET quenching by the bipyridinium units. Reduction of the oxidized chromophore by the Na_2EDTA electron donor, and the concomitant ET from the reduced bipyridinium units to the conductive Au-nanoparticles, and from them to the electrode, leads to the observed photocurrent, Fig. 10(C). Biasing the electrode potential to the negative value that reduces the bipyridinium units to the respective radical cations, blocks the intramolecular ET and the Au-nanoparticle-mediated charge transport to the electrode, and thus the generation of the photocurrent is perturbed. Similar results were observed upon the application of the bis-bipyridinium cyclophane catenated Ru(II)-tris-bipyridine complex, (**5**), Fig. 8. The oligocationic supramolecular complex acts as a crosslinker of the layered Au-nanoparticle array. Photoexcitation of the Ru(II)-tris-bipyridine chromophore results in ET to the threaded bipyridinium cyclophane electron acceptor. Reduction of the oxidized photosensitizer followed by ET from the acceptor to the electrode, through the three-dimensional Au-nanoparticle conductive array, yields the photocurrent, Fig. 11.

4. Photoswitchable electrical transduction of recorded photonic signals using a nitrospiropyran/pyridine monolayer as light recording interface and cytochrome *c*/cytochrome oxidase as biocatalytic transducing cascade

Hemoproteins play a central role in biological processes and act as oxygen or NO carriers, e.g. hemoglobin, ET cofactors, e.g. cytochrome *c* (Cyt. *c*) and bioelectrocatalysts, i.e. cytochrome P-450. The Cyt. *c* cofactor is an interesting hemoprotein as it activates many redox-enzymes by mediated ET. The heme site of Cyt. *c* is shielded towards di-

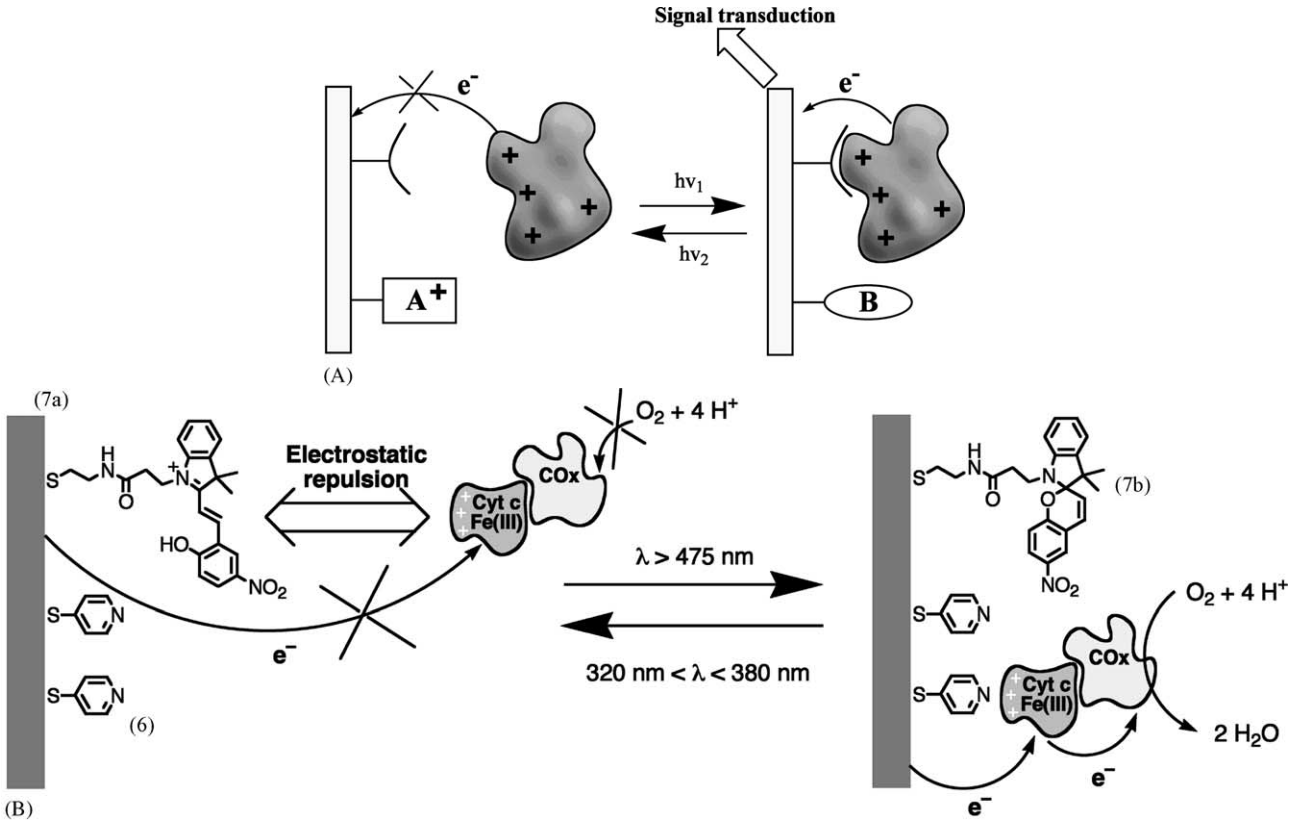

Fig. 12. (A) Photoswitchable 'ON' and 'OFF' activation and deactivation of the electrical contact between a redox protein and an electrode. (B) Photoswitchable activation and deactivation of the electrical contact of Cyt. *c* and an electrode, and of the secondary Cyt. *c*-mediated biocatalyzed reduction of O_2 by COx, using a functional pyridine-nitrospiropyran photoisomerizable mixed monolayer electrode.

rect ET communication with electrode supports. Structural alignment of the Cyt. *c* on electrodes by the site-specific covalent anchoring of the hemoprotein mutants to the conductive support, or the supramolecular binding of the hemoprotein to molecular promoter units associated with the electrode, enabled the establishment of electrical contact between the heme site of Cyt. *c* and the electrode [23].

The ability to control the electrical contact of Cyt. *c* with electrodes by means of surface modifiers, together with the ET functions of Cyt. *c* in the activation of redox-enzymes, turns the hemoprotein into an attractive functional component to design optobioelectronic systems [24,25]. Fig. 12(A) depicts schematically the assembly of an optobioelectronic device based on Cyt. *c* for the amplified amperometric transduction (readout) of recorded photonic information [26]. The electrode is functionalized by a photoactive modifier that undergoes photoisomerization between the states 'A' and 'B'. In state 'A' of the monolayer no affinity interaction between Cyt. *c* and the modifying monolayer exists, and thus Cyt. *c* lacks electrical communication with the electrode. Photoisomerization of the monolayer to state 'B' results in the affinity binding of Cyt. *c* to the electrode. The structural alignment of the hemoprotein on the electrode surface activates the electrical contact and communication between the heme site and the electrode. Further photoisomerization of the monolayer, at a second wavelength ($h\upsilon_2$), restores the monolayer in state 'A', resulting in the dissociation of Cyt. *c* from the electrode, and the blocking of its electrical communication with the electrode. Thus, the optical activation of the electrical communication between the Cyt. *c* and the electrode in the system yields 'Write' and 'Read' functionalities of the assembly, whereas the secondary back isomerization and dissociation of Cyt. *c* from the electrode represents the 'Erase' function of the system. The electrical contact between Cyt. *c* and the electrode in configuration 'B', allows the secondary Cyt. *c*-mediated activation of an enzyme cascade. For example, reduced Cyt. *c* could mediate the ET to cytochrome oxidase (COx) and the activation of the biocatalyzed reduction of O_2 to H_2O. As a limited number of photons affects the photoisomerization of the monolayer to state 'B' that activates the biocatalyzed reduction of O_2 to water, and the formation of numerous product molecules as a result of the photonic process, the latter electron-transfer process represents the amplified electronic transduction of the recorded photonic information. Thus, the photoisomerizable monolayer associated with the electrode acts as a 'command interface' for the photoswitchable control of the electrical communication between Cyt. *c* and the electrode.

A system that enables the photoswitchable activation and deactivation of Cyt. *c* is depicted in Fig. 12(B). A mixed monolayer consisting of mercaptopyridine (**6**) and the photoactive protonated nitromerocyanine units, (**7a**)

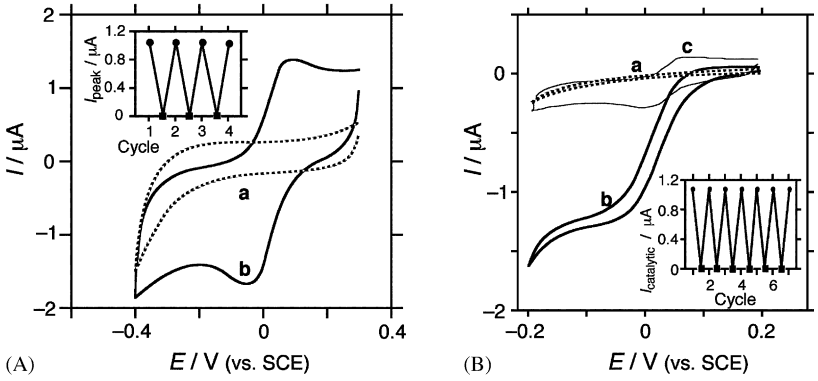

Fig. 13. (A) Cyclic voltammograms of Cyt. *c* in the presence of: (a) The pyridine-protonated nitromerocyanine mixed monolayer-functionalized electrode. (b) The pyridine-nitrospiropyran monolayer-functionalized electrode. *Inset:* cyclic 'ON' and 'OFF' activation of the electrical contact of Cyt. *c* and the electrode by the reversible photoisomerization of the mixed monolayer. (B) Cyclic voltammograms corresponding to: (a) The electrical response of the system consisting of Cyt. *c* and COx under oxygen in the presence of the pyridine-protonated nitromerocyanine monolayer-functionalized electrode. (b) The system consisting of Cyt. *c* and COx under oxygen in the presence of the pyridine-nitrospiropyran-functionalized electrode. (c) The system consisting of Cyt. *c* only in the presence of the pyridine–nitrospiropyran-functionalized electrode. *Inset:* Cyclic photoswitchable amperometric responses of the Cyt. *c*/COx/O_2 system upon the reversible photoisomerization of the mixed monolayer-functionalized electrode.

was assembled on an Au-electrode. At neutral pH, Cyt. *c* is positively-charged, and thus is electrostatically repelled from the electrode surface. Consequently, Cyt. *c* lacks electrical communication with the electrode, and its redox activity is switched-off. Photoisomerization of the monolayer to the nitrospiropyran(**7b**)/mercaptopyridine composite results in a neutral monolayer interface. As pyridine is known to act as a molecular promoter for the redox-activation of Cyt. *c*, the association of Cyt. *c* to the pyridine sites is anticipated to align Cyt. *c* on the electrode, and to switch-on the redox functions of the hemoprotein. Subsequent photoisomerization of the monolayer to the mercaptopyridine/protonated nitromerocyanine state, (**7a**), is expected to result in the electrostatic repulsion of Cyt. *c* from the electrode, and the blocking of its electrical contact with the electrode. Fig. 13(A), curve (a), shows the cyclic voltammogram of the electrode functionalized by the composite mercaptopyridine-protonated nitromerocyanine monolayer in the presence of Cyt. *c*. No electrical response of the heme site is detected, consistent with the electrostatic repulsion of Cyt. *c* from the electrode. The electrode was then photoisomerized, $\lambda > 475$ nm, to the mercaptopyridine-nitrospiropyran state, (**7b**). Fig. 13(A), curve (b), shows the cyclic voltammogram of the modified electrode in the presence of Cyt. *c*. The quasi-reversible redox-wave at $E^\circ = 0.012$ V, indicates that the heme site exhibits effective electrical communication with the electrode. Further irradiation of the monolayer, $320 < \lambda < 380$ nm, results in its back isomerization to the mercaptopyridine-protonated merocyanine, (**7a**), configuration. Formation of the positively-charged interface results in the dissociation of the hemoprotein from the pyridine sites, and the disappearance of the electrical communication between Cyt. *c* and the electrode. By the cyclic photoisomerization of the monolayer between the protonated nitromerocyanine state, (**7a**), and the nitrospiropyran configuration, (**7b**), the electrical response of the hemoprotein can be reversibly switched between the 'OFF' and 'ON' states, respectively, Fig. 13(A), inset. Since Cyt. *c* acts as an ET mediating cofactor to different redox-proteins, the electrically contacted Cyt. *c* configuration may be coupled to the activation of an enzyme cascade. The activation of a biocatalytic process represents an amplification route since the photonic activation of the command monolayer interface by a limited number of photons results in the formation of numerous product molecules by the biocatalytic process. Accordingly, COx, was included as the biocatalyst that reduces O_2 to water. It is known that COx by itself lacks direct electrical contact with electrode surfaces, but Cyt. *c* mediates ET to COx, and activates the enzyme towards the reduction of O_2. Thus, in the presence of the mercaptopyridine–nitrospiropyran (**7b**) monolayer, where the redox functions of Cyt. *c* are switched-on, the mediated reduction of COx is feasible, resulting in the biocatalyzed reduction of O_2 to H_2O_2, Fig. 12(B). That is, the photonic activation of the monolayer to the mercaptopyridine–nitrospiropyran state (**7b**) allows the vectorial ET in the Cyt. *c*/COx/O_2 system, a process that leads to the amplified amperometric transduction of the recorded photonic stimuli. On the other hand, in the presence of the mercaptopyridine-protonated nitromerocyanine (**7a**) state of the monolayer, the electrical communication between Cyt. *c* and the electrode is blocked, and thus the secondary activation of the biocatalyzed reduction of O_2 is prohibited. Fig. 13(B), curve (a), shows the cyclic voltammogram of the mercaptopyridine-protonated nitromerocyanine monolayer-electrode in the presence of Cyt. *c* and COx. No electrical response is observed, consistent with the lack of electrical contact between Cyt. *c* and the electrode. The lack of redox activity of Cyt. *c* prohibits the mediated biocatalyzed reduction of O_2, and the biocatalytic cascade is switched-off. Photoisomerization of the monolayer to the nitrospiropyran (**7b**) state results in the electrical

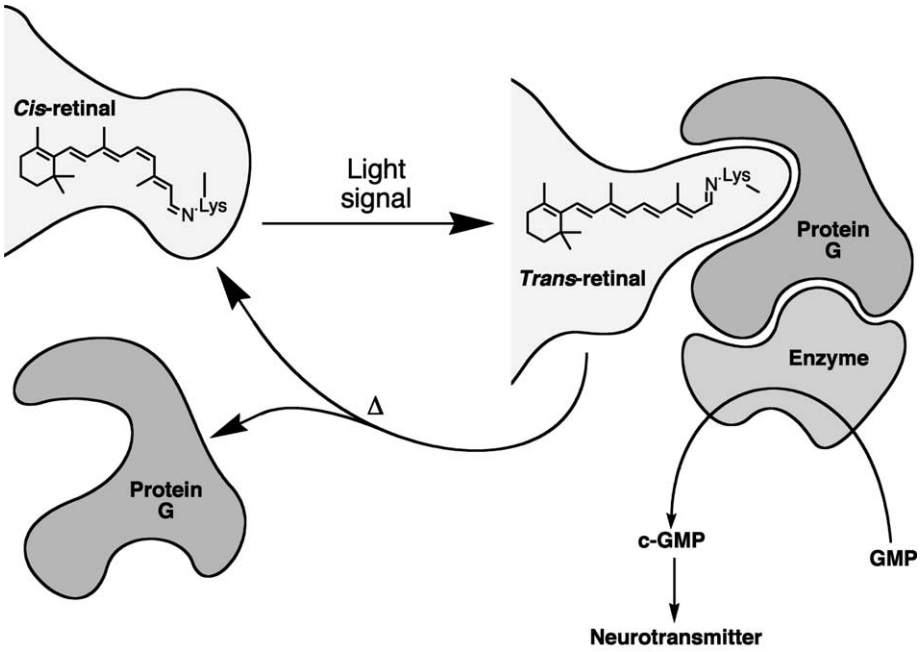

Fig. 14. Schematic photonic activation of the vision process.

communication between Cyt. *c* and the electrode and the secondary activation of the biocatalyzed reduction of O_2 to H_2O. This is evident by the development of an electrocatalytic cathodic current at the redox-potential of Cyt. *c*, Fig. 13(B), curve (b). By the cyclic photoisomerization of the monolayer associated with the electrode between the protonated merocyanine (**7a**) state and the nitrospiropyran configuration (**7b**), the bioelectrocatalytic transformation involving the Cyt. *c*-mediated biocatalyzed reduction of O_2 can be reversibly switched between 'OFF' and 'ON' states, respectively, Fig. 13(B), inset. For comparison, the electrochemical response of the Cyt. *c* under the same experimental conditions, and upon exclusion of COx is depicted in Fig. 13(B), curve (c). Clearly, the coupling of Cyt. *c* to the secondary biocatalyzed cascade that includes COx and O_2 results in an amplified amperometric response due to the electrocatalytic turnover of COx.

The latter system, where the amplified electronic (amperometric) transduction of recorded photonic signals is accomplished by the tailored mercaptopyridine/nitrospiropyran monolayer/Cyt. *c*/COx, O_2, represents an optobioelectronic assembly mimicking the vision process. In the vision process, the retinal chromophore embedded in the membrane undergoes photoisomerization resulting in a structural change in the membrane, Fig. 14. The structural change of the membrane results in the association of Protein G. The bound Protein G activates an enzymatic cascade that transforms GMP to c-GMP that activates the neural response. Thermal relaxation of the chromophore to its original form leads to the dissociation of Protein G and to the blocking of the secondary biocatalyzed generation of c-GMP. Thus, in the artificial system, the photoisomerizable monolayer that includes the pyridine receptor sites, duplicates the functions of the retinal chromophore and the surrounding membrane. Cyt. *c* mimics the functions of Protein G in the activation of the enzyme cascade. The secondary COx/O_2 system acts as the biocatalytic amplification unit that generates current, instead of c-GMP, the neurotransmitter, in the native vision process.

5. Conclusions

The present article has demonstrated means to tailor directional (vectorial) ET reactions in tailored protein assemblies and supramolecular architectures of nanoparticle arrays. The understanding of the fundamental mechanistic feature of ET in these systems enabled us to develop new photocatalytic protein assemblies, organized arrays for photoelectrochemistry, and optoelectronic systems for optical recording and processing. The study has demonstrated that the incorporation of photosensitizer–electron relay units in proteins leads to the effective stabilization of photoinduced ET products against back ET. The stabilization of the photogenerated redox species against recombination enables the use of the reactive species for subsequent chemical transformations. Specifically, the incorporation of Co(II)-protoporphyrin IX, acting simultaneously as electron acceptor site and catalytic unit, into apo-β-hemoglobin and the site-specific covalent anchoring of the eosin chromophore to the protein has led to the preparation of a photoenzyme that stimulated the photochemical hydrogenation of acetylenes. A different concept for utilizing vectorial ET in a protein assembly involved the development of an optobioelectronic system where photonic signals recorded by the system are electronically transduced

and amplified by a biocatalytic ET cascade. The system revealed Write–Read–Erase functionalities and it may be considered as an optobioelectronic system for optical information storage and processing.

Finally, the assembly of layered arrays consisting of molecular crosslinked Au-nanoparticles on transparent ITO electrodes was discussed. The layered structures reveal three-dimensional conductivity and tunable optical properties. By the crosslinking of the Au-nanoparticle layers with photosensitizer–electron-acceptor units, functional arrays with tunable and controlled photoelectrochemical functions were tailored.

The different systems introduce new facets to the rapidly developing areas of nanobiotechnology and nanotechnology. Proteins functionalized with molecular units, supramolecular complexes and functionalized nanoparticles, provide building units that, upon integration with surfaces or electronic transducers, will yield 'smart devices' with novel photocatalytic, optoelectronic, photoelectrochemical and sensoric functions.

Acknowledgements

Parts of this study were supported by the US–Israel Binational Science Foundation (BSF).

References

[1] J. Deisenhofer, H. Michel, in: M.E. Michel-Beyerle (Ed.), Antennas and Reaction Center of Photosynthetic Bacteria, Springer, Berlin, Heidelberg, 1985, p. 94.
[2] (a) J. Deisenhofer, O. Epp, K. Miki, R. Huber, H. Michel, Nature 318 (1985) 618;
(b) C.-H. Chang, D. Tiede, J. Tang, U. Smith, J. Norris, M. Schiffer, FEBS Lett. 205 (1986) 82.
[3] (a) I. Willner, B. Willner, in: D.C. Neckers, D.H. Volman, G. von Bünau (Eds.), Advances in Photochemistry, vol. 20, Wiley, New York, 1995, p. 217;
(b) H. Kurreck, M. Huber, Angew. Chem. Int. Ed. Engl. 34 (1995) 849.
[4] D. Gust, T.A. Moore, A.L. Moore, G. Seely, P. Liddell, D. Barett, L.O. Harding, X.L. Ma, S.J. Lee, F. Gao, Tetrahedron 45 (1989) 4867.
[5] M.R. Wasielewski, Chem. Rev. 92 (1992) 435.
[6] (a) D.M. Guldi, Chem. Soc. Rev. 31 (2002) 22;
(b) C. Luo, D.M. Guldi, H. Imahori, K. Tamaki, Y. Sakata, J. Am. Chem. Soc. 122 (2000) 6535;
(c) H. Imahori, D.M. Guldi, K. Tamaki, Y. Yoshida, C. Luo, Y. Sakata, S. Fukuzumi, J. Am. Chem. Soc. 123 (2001) 6617.
[7] N.J. Turro, M. Grätzel, A.M. Braun, Angew. Chem. Int. Ed. Engl. 19 (1980) 675.
[8] (a) D. Mandler, Y. Degani, I. Willner, J. Phys. Chem. 88 (1984) 4366;
(b) E. Joselevich, I. Willner, J. Phys. Chem. 99 (1995) 6903.
[9] (a) Y. Degani, I. Willner, J. Am. Chem. Soc. 105 (1983) 6228;
(b) I. Willner, J.M. Yang, J.W. Otvos, M. Calvin, J. Phys. Chem. 85 (1981) 3277.
[10] (a) T.L. Pettit, M.A. Fox, J. Phys. Chem. 90 (1986) 1353;
(b) J.S. Krueger, J.E. Mayer, T.E. Mallouk, J. Am. Chem. Soc. 110 (1988) 823.
[11] (a) G. McLendon, Acc. Chem. Res. 21 (1988) 160;
(b) J.R. Winkler, H.B. Gray, Chem. Rev. 92 (1992) 369;
(c) S.E. Peterson-Kennedy, J.L. McGourty, P.S. Ho, C.J. Sutoris, N. Liang, H. Zemel, N.V. Blough, E. Margoliash, B.M. Hoffman, Coord. Chem. Rev. 64 (1985) 125.
[12] (a) N. Liang, A.G. Mauk, G.J. Pielak, J.A. Johnson, M. Smith, B.M. Hoffman, Science 240 (1988) 311;
(b) D.N. Beratan, J.N. Betts, J.N. Onuchic, Science 252 (1991) 1285;
(c) H.B. Gray, J.R. Winkler, Annu. Rev. Biochem. 65 (1996) 537.
[13] (a) J.R. Winkler, A.J. Di Bilio, N.A. Farrow, J.H. Richards, H.B. Gray, Pure Appl. Chem. 71 (1999) 1753;
(b) H.B. Gray, J.R. Winkler, D. Wiedenfeld, Coord. Chem. Rev. 200 (2000) 875.
[14] (a) I. Willner, B. Willner, Top. Curr. Chem. 159 (1991) 153;
(b) I. Willner, E. Zahavy, Angew. Chem. Int. Ed. Engl. 33 (1994) 581.
[15] V. Heleg-Shabtai, T. Gabriel, I. Willner, J. Am. Chem. Soc. 121 (1999) 3220.
[16] (a) I. Willner, E. Zahavy, V. Heleg-Shabtai, J. Am. Chem. Soc. 117 (1995) 542;
(b) E. Zahavy, I. Willner, J. Am. Chem. Soc. 117 (1995) 10581.
[17] (a) I. Hamachi, S. Tanaka, S. Shinkai, J. Am. Chem. Soc. 115 (1993) 10458;
(b) I. Hamachi, S. Tanaka, S. Tsukiji, S. Shinkai, S. Oishi, Inorg. Chem. 37 (1998) 4380;
(c) I. Hamachi, S. Tsukiji, S. Tanaka, S. Shinkai, Chem. Lett. (1996) 751.
[18] A.N. Shipway, E. Katz, I. Willner, ChemPhys Chem. 1 (2000) 18.
[19] A.N. Shipway, I. Willner, Chem. Commun. (2001) 2035.
[20] M. Lahav, R. Gabai, A.N. Shipway, I. Willner, Chem. Commun. (1999) 1937.
[21] (a) M. GrätzelNanocrystalline electronic junctions, in: P.V. Kamat, D. Meisel (Eds.), Semiconductor Nanoclusters-Physical, Chemical and Catalytic Aspects, Elsevier, Amsterdam, 1997, p. 353;
(b) P.V. Kamat, in: J. Fendler (Ed.), Nanoparticles and Nanostructural Films, Wiley-VCH, Weinheim, 1998, p. 207.
[22] (a) M. Lahav, T. Gabriel, A.N. Shipway, I. Willner, J. Am. Chem. Soc. 121 (1999) 258;
(b) M. Lahav, V. Heleg-Shabtai, J. Wasserman, E. Katz, I. Willner, H. Dürr, Y.-Z. Hu, S.H. Bossmann, J. Am. Chem. Soc. 122 (2000) 11480.
[23] (a) F.A. Armstrong, H.A.O. Hill, N.J. Walton, Acc. Chem. Res. 21 (1988) 407;
(b) F.A. Armstrong, H.A.O. Hill, N.J. Walton, Quart. Rev. Biophys. 18 (1986) 261.
[24] I. Willner, Acc. Chem. Res. 30 (1997) 347.
[25] I. Willner, S. Rubin, Angew. Chem. Int. Ed. Engl. 35 (1996) 367.
[26] M. Lion-Dagan, E. Katz, I. Willner, J. Chem. Soc. Chem. Commun. (1994) 2741.